

Boosting spatial resolution by incorporating periodic boundary conditions into single-distance hard-x-ray phase retrieval

David M. Paganin

School of Physics and Astronomy, Monash University, Victoria 3800, Australia

Vincent Favre-Nicolin, Alessandro Mirone, Alexander Rack, Julie Villanova
The European Synchrotron – ESRF, CS40220, 38043 Grenoble, France

Margie P. Olbinado

Paul Scherrer Institut, Forschungsstrasse 111, 5232 Villigen PSI, Switzerland

Vincent Fernandez

The Natural History Museum, Cromwell Road, London SW7 5BD, United Kingdom

Julio C. da Silva

The European Synchrotron – ESRF, CS40220, 38043 Grenoble, France and NEEL Institute CNRS/UGA, 38042 Grenoble, France

Daniele Pelliccia

Instruments & Data Tools Pty Ltd, Victoria 3178, Australia

(Dated: June 18, 2022)

A simple coherent-imaging method due to Paganin *et al.* is widely employed for phase–amplitude reconstruction of samples using a single paraxial x-ray propagation-based phase-contrast image, provided the sample-to-detector distance is sufficiently small for the associated Fresnel number to be large compared to unity. The algorithm is particularly effective when employed in a tomographic setting, using a single propagation-based phase-contrast image for each projection. Here we develop a simple extension of the method, which improves the reconstructed contrast of very fine sample features. This provides first-principles motivation for boosting fine spatial detail associated with high Fourier frequencies, relative to the original method, and was inspired by several recent works employing empirically-obtained Fourier filters to a similar end.

I. INTRODUCTION

In 2002 a simple algorithm was published for reconstructing the projected thickness of a single-material sample given a single propagation-based phase contrast image obtained in the small-defocus regime [1]. In this method, the ratio of the real part of the projected refractive index decrement and the projected linear attenuation coefficient is assumed to be both known and constant. The method assumes paraxial coherent radiation or matter waves (e.g. x-rays, visible light, electrons or neutrons), plane-wave illumination of known intensity, and an object-to-detector propagation distance that is sufficiently small for each structure in the sample to produce no more than one Fresnel fringe (more precisely, the object-to-detector distance is assumed to be small enough to make the corresponding Fresnel number large compared to unity). Within its domain of validity (single-material sample and small object-to-detector propagation distance for paraxial radiation or matter waves), the method may be viewed as providing a computationally-simple unique closed-form deterministic solution to the twin-image problem of inline holography [2], since propagation-based phase contrast images are synonymous with inline holograms [3].

The 2002 algorithm has been widely utilised, particularly for propagation-based x-ray phase contrast imaging. Its advantages, bought at the price of the previously stated strong assumptions, include simplicity, speed, significant noise robustness even for strongly absorbing samples, and the ability to process time-dependent images frame-by-frame. Efficient computer implementations are available in the following software packages: ANKAphase [4], X-TRACT [5], pyNX [6], PITRE [7], Octopus [8, 9], pyHST2 [10], TomoPy [11, 12], SYRMEP Tomo Project [13] and HoloTomo Toolbox [14]. While most applications to date have employed x-rays, the method was originally developed with a broader domain of applicability in mind, including but not limited to electrons, visible light and neutrons [1]. Subsequently, the method has now also been applied to out-of-focus contrast images obtained using electrons [15], visible light [16] and neutrons [17].

When the method of Paganin *et al.* [1] (PM) is utilised in a tomographic context [18], its domain of utility broadens since many objects may be viewed as locally composed of a single material of interest, in three spatial dimensions, even though they cannot be described as composed of a single material in projection [19, 20]. Early examples of applications of the PM in a tomographic setting include the imaging of paper [18], polymer micro-wire composites [21], high-Weber-number water jets [22], self

healing thermoplastics [23], paint-primer micro-structure [24], partially open foams [25], sandstone micro-structure [26], granite [27], melting snow [28], anthracite coal [29], evolving liquid foams [30], iron oxide particles in mouse brains [31, 32], rat brains [20], mouse lungs [33], rabbit lungs [20], mouse tibiae [34], crocodile teeth [35], mosquitoes [4], fly legs [18], high speed *in vivo* imaging of a fly's flight motor system [36], wood [21], dynamic crack propagation in heat treated hardwood [37], rose peduncles [38], amber-fossilised spiders [39, 40], amber-fossilised centipedes [41], fossilised rodent teeth [42], fossil bones [43], ancient cockroach coprolites [44], fossilised early-animal embryos [45], fossil muscles of primitive vertebrates [46, 47] and the vertebral architecture of ancient tetrapods [48]. Publications from 2014 onwards to the present are too numerous to list [49].

The present work was inspired by several publications that incorporate unsharp masking or related techniques to boost fine spatial detail in reconstructions obtained using the PM. This includes the deconvolution filter incorporated into the ANKAphase [4] version 2.1 implementation of the PM, Sanchez *et al.*'s incorporation of an unsharp mask into the pyHST2 implementation of the PM [10, 43], and the work of Irvine *et al.* [50] utilising the measured phase contrast image as a physical unsharp mask. These extensions of the method all suppress high spatial-frequency information by a factor less than that given by the Fourier-space Lorentzian [51] filter that is employed in the PM. Notable also is the work of Yu *et al.* [52], which enhances fine spatial detail by adapting the PM to a multi-image setting. The resulting improvements, most particularly in fine spatial detail obtained via tomographic reconstructions utilising the method, are clearly evident in the previously cited publications. These publications [4, 10, 47, 50, 52] provide impetus to revisit the theory underpinning the PM, thereby seeking a first-principles justification for reduced suppression of high spatial frequency information, relative to the Fourier filter in the original form of the method.

The remainder of the paper is structured as follows. Section II derives a generalised form of the PM ("GPM"), showing how it reduces to the original form of the single-image phase-retrieval algorithm for low spatial frequencies in the input phase-contrast image data. Simulated x-ray data is considered in Sec. III, comparing the GPM to the PM, and exploring the limits of both approaches. Section IV discusses the domain of applicability for both the GPM and the PM, together with the effective high-pass filter to the PM that is implied by the GPM. Section V indicates some possible possible avenues for future work. We conclude with a brief summary in Sec. VI.

II. INCORPORATION OF PERIODIC BOUNDARY CONDITIONS INTO THE PM

For a monochromatic scalar x-ray wavefield with intensity $I(x, y, z)$ and phase $\varphi(x, y, z)$ that is paraxial with

respect to an optical axis z , the associated continuity equation is known as the transport-of-intensity equation [53] (TIE):

$$\nabla_{\perp} \cdot [I(x, y, z) \nabla_{\perp} \varphi(x, y, z)] = -k \frac{\partial I(x, y, z)}{\partial z}. \quad (1)$$

Here, (x, y) denote Cartesian coordinates in planes perpendicular to the optical axis, ∇_{\perp} denotes the gradient operator in the xy plane and $k = 2\pi/\lambda$ is the wavenumber corresponding to the vacuum wavelength λ . A validity condition for this equation is that the Fresnel number N_F obey

$$N_F \equiv \frac{W^2}{\lambda \Delta} \gg 1. \quad (2)$$

Here, W is the characteristic transverse length scale for the wavefield being propagated, and $\Delta \geq 0$ is the distance from (i) the planar exit surface $z = 0$ over which the unpropagated wavefield is specified, to (ii) the parallel planar surface $z = \Delta$ over which the intensity of the propagated wavefield is registered using a pixellated position-sensitive detector (see Fig. 1.)

Following Paganin *et al.* [1], consider a single-material object lying immediately upstream of the plane $z = 0$, whose z -projection of thickness is given by $T(x, y)$ – see Fig. 1. The projection approximation [54] gives the usual Beer–Lambert law for the intensity $I(x, y, z = 0)$ at the exit surface $z = 0$ of the object, for the case where the object is illuminated with z -directed monochromatic plane waves having uniform intensity I_0 :

$$I(x, y, z = 0) = I_0 \exp[-\mu T(x, y)]. \quad (3)$$

Here, μ is the linear attenuation coefficient of the object. The projection approximation also gives an expression for the transverse phase distribution over the exit surface of the object [54]:

$$\varphi(x, y, z = 0) = -k\delta T(x, y), \quad (4)$$

where $1 - \delta$ is the real part of its complex refractive index

$$n = 1 - \delta + i\beta \quad (5)$$

and

$$\mu = 2k\beta. \quad (6)$$

Note that the single-material object may be generalised to the case of variable mass density $\rho(x, y, z)$, the requirement then being that its complex refractive index have the form

$$n(x, y, z) = 1 - A\rho(x, y, z), \quad (7)$$

where A is a fixed complex constant at fixed energy, and $\text{Re}A > 0$ [55].

Assume vacuum to lie in the half space $z \geq 0$ downstream of the object. Assume the exit-surface wavefield over the plane $z = 0$ to propagate through a distance $\Delta > 0$ downstream of the object, with this distance being sufficiently small for the Fresnel number

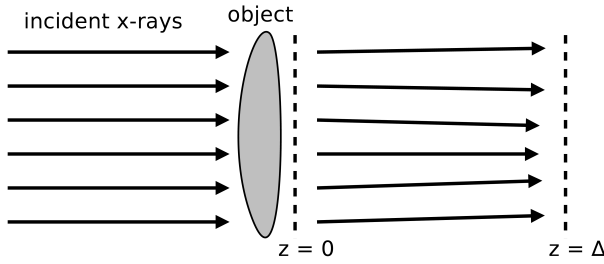


FIG. 1. A single-material object of projected thickness $T(x, y)$ is illuminated by normally incident z -directed monochromatic scalar plane waves of uniform intensity I_0 , where (x, y) are Cartesian coordinates perpendicular to the optical axis z . The resulting paraxial exit-surface wavefield, over the plane $z = 0$, propagates in vacuum through a distance $z = \Delta$. The associated propagation-based phase contrast image has intensity distribution $I(x, y, z = \Delta)$.

to be much greater than unity. We may then make the following forward-finite-difference approximation to the longitudinal intensity derivative on the right side of Eq. (1), using the propagation based phase contrast image $I(x, y, z = \Delta)$ of the single-material object in tandem with the estimate for the contact image given by Eq. (3):

$$\frac{\partial I(x, y, z)}{\partial z} \Big|_{z=0} \approx \frac{I(x, y, z = \Delta) - I_0 \exp[-\mu T(x, y)]}{\Delta}. \quad (8)$$

If Eqs (3), (4) and (8) are substituted into Eq. (1), rearrangement yields the screened Poisson equation [1]:

$$\frac{I(x, y, z = \Delta)}{I_0} = \left(1 - \frac{\delta \Delta}{\mu} \nabla_{\perp}^2\right) \exp[-\mu T(x, y)]. \quad (9)$$

Here, $h(x, y)$ is a twice-differentiable continuous single-valued function, sampled over a mesh in which each grid element is a square of physical width W metres by W metres. Hence the mesh locations are given by

$$(x_m, y_n) = (Wm, Wn), \quad (12)$$

where m and n are integers (mesh indices) that are restricted to the ranges $0 \leq m \leq N_1 - 1$ and $0 \leq n \leq N_2 - 1$,

The manner in which this has been previously solved is to notice that Fourier transformation turns this partial differential equation into an algebraic equation, via the Fourier derivative theorem. This leads immediately to the PM [1]:

$$T(x, y) = -\frac{1}{\mu} \log_e \left(\mathcal{F}^{-1} \left\{ \frac{\mathcal{F}[I(x, y, z = \Delta)/I_0]}{1 + (\delta \Delta/\mu)(k_x^2 + k_y^2)} \right\} \right). \quad (10)$$

Here \mathcal{F} denotes Fourier transformation with respect to x and y in any convention for which ∇_{\perp} transforms to (ik_x, ik_y) , \mathcal{F}^{-1} is the corresponding inverse Fourier transformation, and (k_x, k_y) are Fourier-space spatial frequencies corresponding to (x, y) . The Fourier-space filter, in the above expression, has the previously-mentioned Lorentzian form.

When Eq. (10) is directly applied to experimental propagation-based x-ray phase contrast images that are sampled over a Cartesian mesh, and the discrete Fourier transform used to approximate the (continuous) Fourier transform integral, there is an implicit assumption that the object does not contain appreciable spatial frequency information in the vicinity of the Nyquist limit of the mesh. While this assumption was once typically quite reasonable in most coherent-x-ray-imaging contexts, the exquisitely detailed structures that are now routinely imaged in contemporary x-ray phase-contrast-tomography applications imply that this implicit assumption may now be becoming somewhat less broadly applicable—see e.g. Sanchez *et al.* [43]. For such applications, and as the following argument will demonstrate, Eq. (10) overly strongly filters the highest spatial-frequency information that is present in the data.

With a view to extending the validity of the PM out to the Nyquist limit of the data sampled on a typical pixelated imaging-detector array, recall the following five-point approximation for the transverse Laplacian [56, 57]:

$$\nabla_{\perp}^2 h(x_m, y_n) = \frac{h(x_{m-1}, y_n) + h(x_{m+1}, y_n) + h(x_m, y_{n-1}) + h(x_m, y_{n+1}) - 4h(x_m, y_n)}{W^2}. \quad (11)$$

with N_1 being the number of sample points in the x direction, and N_2 being the number of sample points in the y direction. The key point, here, is that while the fundamental-calculus definition of the transverse derivative considers the mesh step-size W to tend to zero, when working with a discrete grid we are not justified in taking W to be any smaller than the pixel size of the mesh.

With the specified mesh of pixel locations (x_m, y_n) in place, the function $h(x_m, y_n)$ may be expressed in terms of its discrete Fourier transform $H(k_{x,p}, k_{y,q})$ [56]:

$$h(x_m, y_n) = \frac{1}{N_1 N_2} \sum_{p=0}^{N_1-1} \sum_{q=0}^{N_2-1} \exp \left(-\frac{2\pi i m p}{N_1} \right) \exp \left(-\frac{2\pi i n q}{N_2} \right) H(k_{x,p}, k_{y,q}). \quad (13)$$

Here, the discreteness of the sampling grid restricts the allowed spatial frequencies (k_x, k_y) to the mesh

$$(k_{x,p}, k_{y,q}) = \left(\frac{2\pi p}{N_1 W}, \frac{2\pi q}{N_2 W} \right), \quad (14)$$

with p lying in the range $-\frac{1}{2}N_1, \dots, \frac{1}{2}N_1$, and q lying in the range $-\frac{1}{2}N_2, \dots, \frac{1}{2}N_2$.

Motivated by the form of the differential operator in Eq. (9), we can show by direct substitution of Eq. (13) into Eq. (11) that (cf. Freischlad and Koliopoulos [58], Ghiglia and Romero [59] and Arnison *et al.* [60]):

$$(1 - \alpha \nabla_{\perp}^2) h(x_m, y_n) = \frac{1}{N_1 N_2} \sum_{p=0}^{N_1-1} \sum_{q=0}^{N_2-1} \exp\left(-\frac{2\pi i p}{N_1}\right) \exp\left(-\frac{2\pi i n}{N_2}\right) H(k_{x,p}, k_{y,q}) \\ \times \left\{ 1 - \frac{2\alpha}{W^2} \left[\cos\left(\frac{2\pi p}{N_1}\right) + \cos\left(\frac{2\pi q}{N_2}\right) - 2 \right] \right\}, \quad (15)$$

where α is a constant having dimensions of squared length. Set this constant to the real non-negative number:

$$\alpha = \frac{\delta\Delta}{\mu}. \quad (16)$$

Equation (15) then implies that Eq. (9) may be solved for the projected thickness $T(x, y)$ of the single-material sample, over the lattice of points (x_m, y_n) , via the following generalised form of the PM (termed the “GPM” henceforth):

$$T(x_m, y_n) = -\frac{1}{\mu} \log_e \left(\text{IDFT}_{q \rightarrow n}^{p \rightarrow m} \left\{ \frac{\text{DFT}_{n \rightarrow q}^{m \rightarrow p} [I(x_m, y_n, z = \Delta) / I_0]}{1 - \frac{2\alpha}{W^2} [\cos(Wk_{x,p}) + \cos(Wk_{y,q}) - 2]} \right\} \right), \quad \alpha = \frac{\delta\Delta}{\mu}, \quad |Wk_{x,p}|, |Wk_{y,q}| \leq \pi. \quad (17)$$

Here, $\text{DFT}_{n \rightarrow q}^{m \rightarrow p}$ is the discrete Fourier transform operator, which maps a function $h(x_m, y_n)$ sampled on the real-space lattice (x_m, y_n) to its discrete Fourier transform $H(k_{x,p}, k_{y,q})$ sampled on the Fourier-space lattice $(k_{x,p}, k_{y,q})$, and $\text{IDFT}_{q \rightarrow n}^{p \rightarrow m}$ is the corresponding inverse discrete Fourier transform (cf. Eq. (13); cf. Ghiglia and Romero [59], who write a similar expression in the context of the Poisson equation). Note that the key parameter in the above equation is the dimensionless constant:

$$\frac{\alpha}{W^2} = \frac{\delta/\beta}{4\pi N_F}. \quad (18)$$

Several plots of the low-pass Fourier-space filter in Eq. (17) are given in Fig. 2, as a function of the single dimensionless parameter α/W^2 . Note the transition from (i) near-rotational-symmetry and near-Lorentzian form close to the origin of Fourier space, to (ii) the symmetry of a square at the edges of Fourier space. The filter obeys periodic boundary conditions at the edges of the Fourier-space mesh, with each mesh value along the mesh’s edges corresponding to a Nyquist frequency, namely:

$$Wk_{x,p}^{\max}, Wk_{y,q}^{\max} = \pm\pi. \quad (19)$$

An evident trend is that, while the GPM filter clearly differs from the (rotationally symmetric) PM filter for the smaller values of $\alpha/W^2 \leq 1$ given in Figs. 2(a,b,c),

for the larger values of $\alpha/W^2 > 1$ in Figs. 2(d,e,f) the GPM filter has essentially converged to the PM filter. This relation between the two filters will be explored in further detail below. On a different note, another general trend is evident in Fig. 2, namely the fact that the Fourier-space filtration becomes progressively stronger as the dimensionless parameter α/W^2 increases. This latter trend makes intuitive physical sense, since (i) the stronger the propagation-based phase contrast effects in the image recorded over the plane $z = \Delta$, the greater will be the amplification of encoded high-spatial-frequency detail in the projected thickness of the sample, and hence the greater the degree of Fourier-space filtration that is required in order to decode the phase-contrast signal so as to give the required projected thickness; (ii) the phase-contrast signal is directly proportional to δ/β (see Eq. (9)) and inversely proportional to the Fresnel number N_F (as larger Fresnel numbers correspond to smaller propagation distances Δ and/or more slowly varying transverse structure in the wavefield at the exit surface of the sample), which is precisely the dependence on the right side of Eq. (18).

In the low-spatial-frequency limit, we may make the second-order Taylor-series approximation

$$\cos(Wk_{x,p}) \approx 1 - \frac{1}{2}(Wk_{x,p})^2, \\ \cos(Wk_{y,q}) \approx 1 - \frac{1}{2}(Wk_{y,q})^2. \quad (20)$$

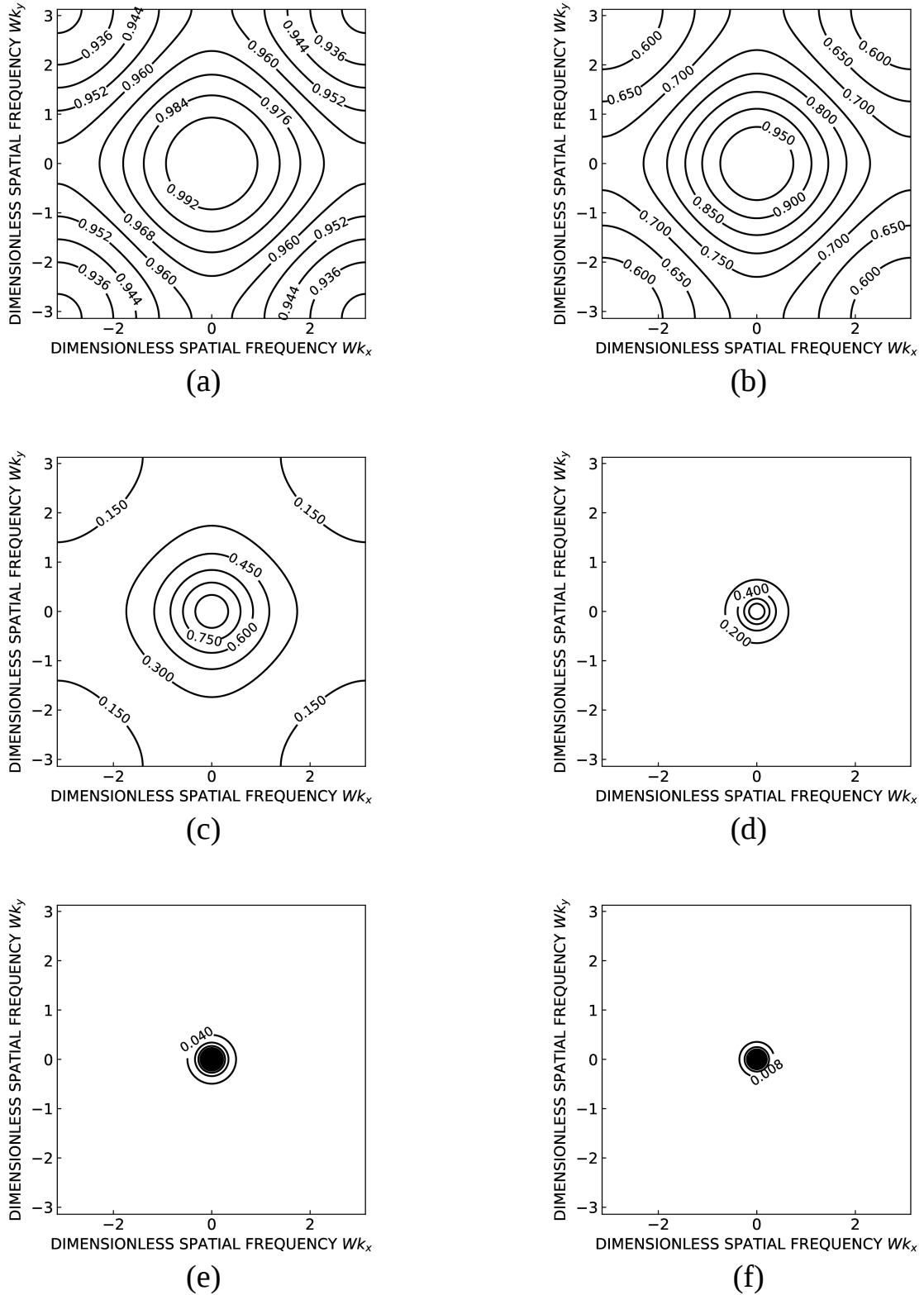


FIG. 2. Contour plot of Fourier-space filter in Eq. (17), over the full discrete Fourier-space range $-\pi \leq Wk_x, Wk_y \leq \pi$, where W is the physical pixel width and $\alpha = \delta\Delta/\mu$. (a) $\alpha/W^2 = 0.01$; (b) $\alpha/W^2 = 0.1$; (c) $\alpha/W^2 = 1.0$; (d) $\alpha/W^2 = 10$; (e) $\alpha/W^2 = 100$; (f) $\alpha/W^2 = 1000$. All plots equal unity at the origin of Fourier space. Note also that $\alpha/W^2 = (4\pi N_F)^{-1} \delta/\beta$.

Equation (17) then reduces to the PM with its

rotationally-symmetric discrete-Fourier-transform representation of Eq. (10) and the associated Lorentzian filter:

$$T(x_m, y_n) \longrightarrow -\frac{1}{\mu} \log_e \left(\text{IDFT}_{q \rightarrow n}^{p \rightarrow m} \left\{ \frac{\text{DFT}_{n \rightarrow q}^{m \rightarrow p}[I(x_m, y_n, z = \Delta)/I_0]}{1 + \alpha (k_{x,p}^2 + k_{y,q}^2)} \right\} \right), \quad \alpha = \frac{\delta \Delta}{\mu}, \quad |Wk_{x,p}|, |Wk_{y,q}| \ll 1. \quad (21)$$

While Eq. (17) (GPM) reduces to Eq. (21) (PM) for low Fourier spatial frequencies, the GPM is less strongly suppressing of high Fourier spatial frequencies. This key point will be explored further in a subsequent section. However, before considering this point in further detail, it is useful first to consider an indicative numerical illustration of the difference between the GPM and PM filters. It is to this latter topic that we now turn.

III. COMPUTER SIMULATIONS

The efficiency of the generalised phase-retrieval reconstruction method can be asserted by simulating paraxial x-ray propagation through a suitably-high-resolution object, and reconstructing it using both the PM and the GPM. To perform this, we chose a spatially random binary object (Fig. 3a) with an x-ray wavelength of 0.5 \AA , $\beta = 10^{-9}$, $\delta = 5 \times 10^{-7}$, a pixel size of 10 \mu m , and a thickness for the object of 40 \mu m . A simulated unit-amplitude plane-wave was transmitted through this object and propagated by a distance of $\Delta = 0.1 \text{ m}$ using a near-field propagator. In order to avoid aliasing effects due to the discrete Fourier transform used, the propagation was performed on a $2 \times$ oversampled object (where the binary random pattern pixels had a 2×2 size), and the propagated intensity was rebinned (averaging the intensity over 2×2 pixels) before being back-propagated. Thus the object-plane image was oversampled and the corresponding propagated intensity subsequently down-sampled to compensate for the initial oversampling of the object.

Figures 3b and 3c show the intensity of the propagated waves reconstructed using the PM and GPM, respectively, where the obtained thickness maps (normalised to the starting object thickness of 40 \mu m) are compared. There is a significant improvement in the reconstructed images obtained with the GPM relative to the images reconstructed with the PM. Figure 3d displays line profiles across the images which indicate improvement in the contrast. Since the low-frequency reconstructed images can be approximated as due to a convolution-induced blurring of the original image, we also performed a Richardson–Lucy deconvolution [61, 62] using the original pattern as a reference, which allows us to estimate the point-spread-function kernel relating the reconstructed and original arrays. Figure 3e shows that the GPM yields a sharper kernel.

IV. DISCUSSION

As stated in the introduction, the work of the present theoretical paper was inspired by several experimental investigations [4, 10, 43, 47, 50] that phenomenologically employ unsharp masks or deconvolution to boost high-spatial-frequency information in x-ray phase contrast tomograms whose reconstructions are obtained with the assistance of the PM. This phenomenological modification to the PM often very significantly improves the level of fine-detail clarity in the reconstructions. Is there a fundamental explanation, derivable from an optical-imaging-physics perspective, that casts some light on why the phenomenological high-frequency-boost strategy is so successful? While we do not claim to give a complete answer to this still-open question, below we argue that the PM-to-GPM transition goes partway to addressing it.

Consider the ratio $R(k_x, k_y)$ of the GPM and PM Fourier-space filters, as given by Eqs (17) and (21):

$$R(k_x, k_y) = \frac{1 + \alpha(k_x^2 + k_y^2)}{1 - \frac{2\alpha}{W^2}[\cos(Wk_x) + \cos(Wk_y) - 2]}, \quad -\pi/W \leq k_x, k_y \leq \pi/W. \quad (22)$$

This ratio may be viewed as a form of deconvolution mask, here derived from first principles, whose application transforms the PM into the GPM. As mentioned earlier in the present paper, such a deconvolution-mask viewpoint may be compared to (and was indeed inspired by) previously-published work which introduced such masks from a phenomenological perspective [4, 10, 43, 50].

The ratio in Eq. (22) is always greater than or equal to unity, implying that the GPM filter (Eq. (17)) suppresses each Fourier component of the measured phase contrast signal, by an amount that is never more than the degree of suppression based on the PM filter (Eq. (21)). To illustrate this point, see Fig. 4 for a series of contour plots of the Fourier-filter-ratio in Eq. (22), for the same range of α/W^2 values that was used in Fig. 2. The form of these plots—which give a GPM-to-PM filter ratio of unity near the Fourier-space origin, and boost high spatial frequencies by taking a value that is progressively greater than unity the further we move away from the Fourier-space origin—gives a partial first-principles justification for the previously cited works boosting high spatial frequencies of tomographic reconstructions based on the PM. However, we must emphasise that the degree

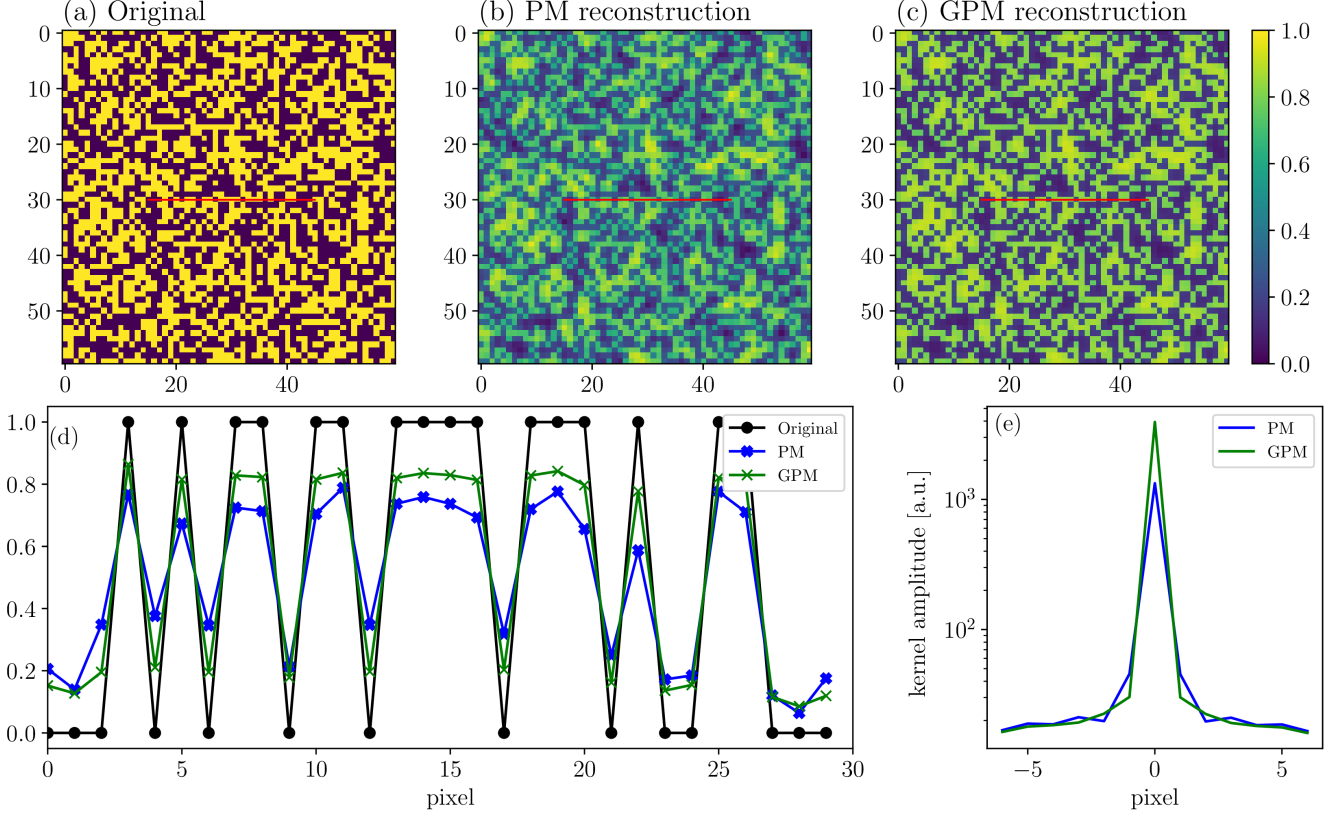


FIG. 3. Simulated reconstructions using (a) a spatially random binary transmission pattern, before propagation and reconstruction using (b) the standard and (c) generalised approach (see text for details). Coordinates are given in pixels. (d) Line profile (indicated by a red line in (a-c)) along the original and reconstructed binary patterns. Both images and line profiles exhibit a higher contrast for the generalised method. (e) Line profile of the kernel obtained using a Richardson–Lucy deconvolution [61, 62] between the original array and each of the back-propagated arrays. The generalised method yields a sharper kernel.

of high-spatial-frequency boost, in the previously cited works [4, 10, 43, 47, 50], is typically significantly larger than the degree of boost that can be justified using the arguments developed in the present paper. It is for this reason that we describe our first-principles justification as “partial”: the GPM gives a reconstruction of fine spatial detail that is superior to that obtained with the PM, but the GPM yields reconstructions that are inferior to those obtained by applying the previously-cited phenomenological approaches [4, 10, 43, 47, 50] to improve the PM by suitably boosting high spatial frequencies. We conjecture there to be an additional factor or factors that can be used to derive additional high-frequency boosts from first principles, but the nature of these factors remains unanswered by the present investigation.

In light of the above comments, let us make some additional remarks regarding the Fourier-filter-ratio plots in Fig. 4. Near the origin of Fourier space, corresponding to coarser spatial detail in the reconstruction, the plots of Fig. 4 have a plateau of values near unity. Again, this is consistent with the GPM reducing to the PM at sufficiently coarse spatial resolution. The maximum value R_{\max} of the ratio $R(k_x, k_y)$, attained at the corners of

the Fourier-space mesh, is given by

$$R_{\max} = \frac{1 + 2\pi^2\Upsilon}{1 + 8\Upsilon}, \quad (23)$$

where

$$\Upsilon \equiv \alpha/W^2 = (4\pi N_F)^{-1}\delta/\beta. \quad (24)$$

When $\Upsilon \gg 1$ (e.g. for sufficiently small W), we see that the maximal Fourier-space boost R_{\max} (of the GPM Fourier filter relative to the PM Fourier filter) is by a factor of $\pi^2/4 \approx 2.5$. Conversely, when $\Upsilon \ll 1$ (e.g. for sufficiently large W), then R_{\max} tends to unity.

If we Taylor expand Eq. (22) to fourth order in spatial frequency, which will be a fair approximation for spatial frequencies that are not too large in magnitude relative to the Nyquist frequency, we obtain

$$R(k_x, k_y) \approx 1 + \frac{1}{12}\alpha W^2(k_x^4 + k_y^4). \quad (25)$$

The fact, that the smallest non-constant term in this expansion is quartic in spatial-frequency coordinates, is consistent with the plateau of values close to unity, exhibited by the plots in Fig. 4 near the Fourier-space origin.

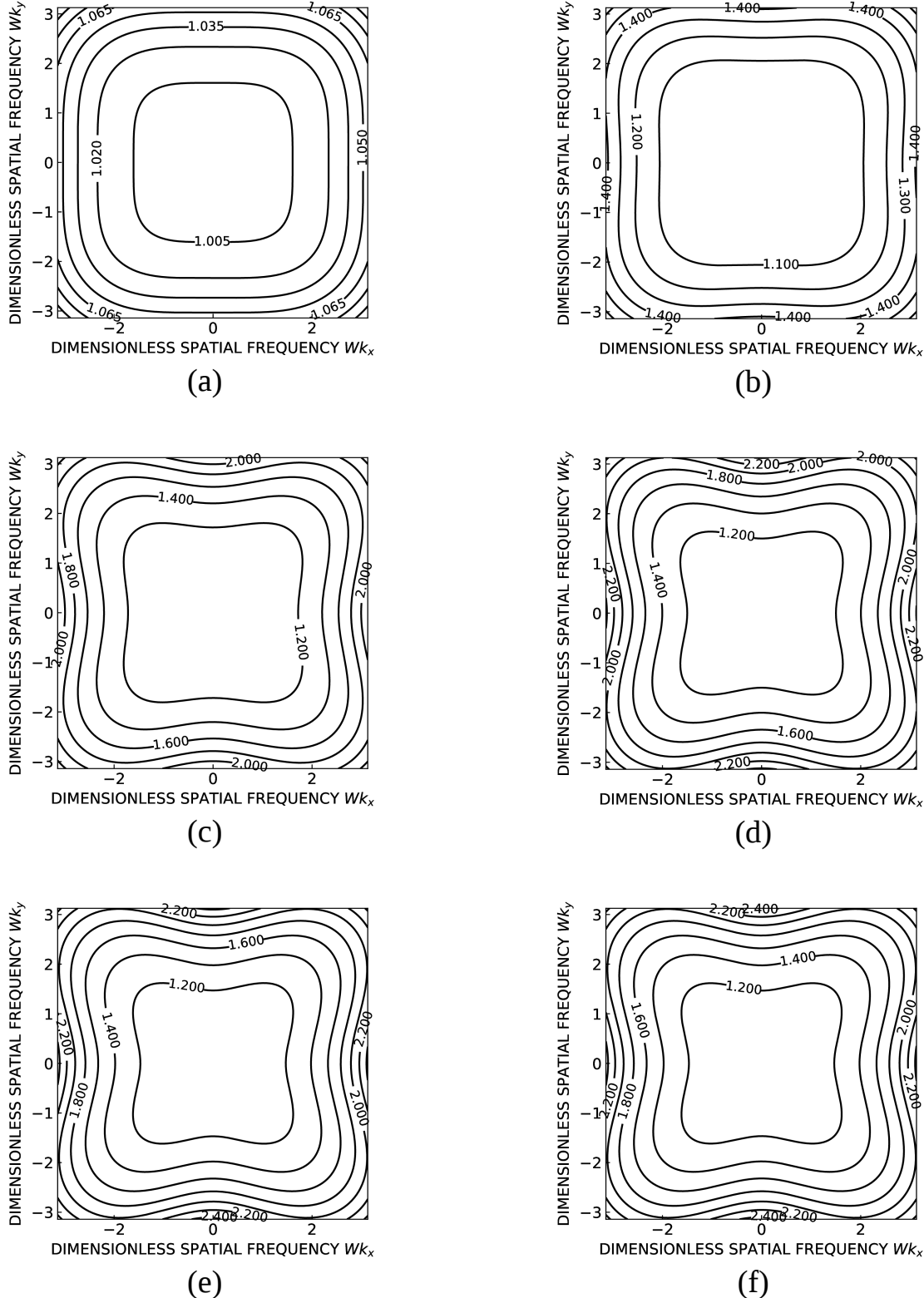


FIG. 4. Contour plot of the ratio of Fourier-space filters given by Eq. (22), over the full discrete Fourier-space range $-\pi \leq Wk_x, Wk_y \leq \pi$, where W is the physical pixel width and $\alpha = \delta\Delta/\mu$. (a) $\alpha/W^2 = 0.01$; (b) $\alpha/W^2 = 0.1$; (c) $\alpha/W^2 = 1.0$; (d) $\alpha/W^2 = 10$; (e) $\alpha/W^2 = 100$; (f) $\alpha/W^2 = 1000$. These plots quantify the degree to which the generalised PM filter amplifies high spatial frequencies, relative to the previously published form of the filter which is valid in the region close to the origin of discrete Fourier space. All plots equal unity at the origin of Fourier space. Note that $\alpha/W^2 = (4\pi N_F)^{-1} \delta/\beta$.

This aligns with the idea that the usual form of the PM works well for coarser spatial detail, but needs the GPM (or some other suitable approach) for better treatment of higher-spatial-frequency detail. The above result also implies that the GPM Fourier filter is approximately equal to $R(k_x, k_y) \approx 1 + \frac{1}{12}\alpha W^2(k_x^4 + k_y^4)$ multiplied by the PM Fourier filter, at least for sufficiently small Fourier frequencies; the corresponding real-space unsharp mask is therefore proportional to the result of applying the non-rotationally-symmetric fourth-order differential operator $\partial^4/\partial x^4 + \partial^4/\partial y^4$ to the PM image, rather than the more usual unsharp mask proportional to the result of applying the rotationally-symmetric second-order differential operator $-(\partial^2/\partial x^2 + \partial^2/\partial y^2)$ to the PM image.

It is interesting to further examine the conditions under which the GPM differs significantly from the PM. Take the ratio of Fourier filters in Eq. (22), and evaluate this ratio at the maximum (Nyquist) x and y spatial frequencies

$$k_x^{\max} = k_y^{\max} = \frac{\pi}{W}. \quad (26)$$

This gives the condition

$$R\left(k_x = \frac{\pi}{W}, k_y = \frac{\pi}{W}\right) = R_{\max} = \frac{1 + \frac{2\alpha\pi^2}{W^2}}{1 + \frac{8\alpha}{W^2}} \geq 1 + \aleph \quad (27)$$

for the GPM to be significantly different in comparison to the PM. Here, \aleph is a lower bound on the maximum relative difference, between the ratio of the two filters and unity, which is considered to be “significant”. Next we (i) make use of Eqs. (6) and (16); (ii) incorporate both the definition of the Fresnel number and its associated requirement as given in Eq. (2). Hence we obtain the following material-dependent parameter domain for which the GPM is both (i) a significant improvement upon the PM, and (ii) still within the domain of validity for the underpinning transport-of-intensity equation:

$$\frac{\delta}{\beta} \left(\frac{\frac{\pi}{2} - \frac{2}{\pi}}{\aleph} - \frac{2}{\pi} \right) \geq N_F \gg 1. \quad (28)$$

Thus e.g. if we choose $\aleph = 0.1$, and round numerical factors to the nearest order of magnitude, the above in-

equalities become the material-dependent conditions:

$$10 \frac{\delta}{\beta} \geq N_F \gg 1. \quad (29)$$

Some sample numerical values may be used to illustrate the above expression: if $\delta/\beta = 500$, $\lambda = 0.5 \text{ \AA} = 0.5 \times 10^{-10} \text{ m}$ and $W = 10 \mu\text{m} = 10^{-5} \text{ m}$, then Eq. (29) will be satisfied if $0.4 \text{ mm} \leq \Delta \ll 2 \text{ m}$. If the pixel size is halved to $W = 5 \mu\text{m}$, leaving all other parameters unchanged, we instead obtain $0.1 \text{ mm} \leq \Delta \ll 50 \text{ cm}$. If the condition in Eq. (28) is violated then more sophisticated methods than either the PM or the GPM will need to be employed, including but not limited to (i) holotomography [63], (ii) approaches based on the first Born and Rytov approximations [64], (iii) approaches based on the contrast-transfer-function formalism [65, 66], and (iv) the variety of approaches that are both reported upon and compared in Yu *et al.* [67].

One further point should be made regarding unsharp masks and deconvolution. The GPM will still benefit from additional unsharp masking or deconvolution, to further boost high-spatial-frequency detail, since—among other reasons that are beyond the scope of the present investigation, such as truncation of the effects of Fresnel diffraction to ignore the presence of multiple Fresnel-diffraction fringing—the GPM does not explicitly take source-size-induced blurring into account. The degree of sharpening required for GPM-reconstructed images will necessarily be less pronounced than that which has been needed for PM-reconstructed images. In this context we point out that the image-blurring effect due to finite source size may be modelled by making the following replacement in Eq. (9) [68]:

$$\frac{\delta}{\mu} \rightarrow \frac{\delta}{\mu} - \frac{2S^2}{\Delta}. \quad (30)$$

Here, S is the radius of the effective incoherent point-spread function at the detector plane, that is due to source-size blurring (cf. Gureyev *et al.* [69]). The above replacement transforms Eq. (9) into a Fokker–Planck form [70–72] for which $2S^2/\Delta$ plays the role of an effective diffusion coefficient [73]. This simple algebraic replacement may be carried through all of the calculations of the present paper, thereby incorporating a partial source-size deconvolution into the analysis.

We close this discussion by observing that we can readily introduce a real parameter τ , which lies between zero and unity inclusive, that may be used to continuously deform the PM algorithm in Eq. (21) ($\tau = 0$), into the GPM algorithm in Eq. (17) ($\tau = 1$), via:

$$T(x_m, y_m) = -\frac{1}{\mu} \log_e \left(\text{IDFT}_{q \rightarrow n}^{p \rightarrow m} \left\{ \frac{\text{DFT}_{n \rightarrow q}^{m \rightarrow p}[I(x_m, y_n, z = \Delta)/I_0]}{1 + \alpha (k_{x,p}^2 + k_{y,q}^2) - \frac{2\alpha\tau}{W^2} \Phi(k_{x,p}, k_{y,q})} \right\} \right), \quad 0 \leq \tau \leq 1, \quad (31)$$

where

$$\Phi(k_{x,p}, k_{y,q}) \equiv \cos(Wk_{x,p}) + \cos(Wk_{y,q}) - 2 + \frac{1}{2}(Wk_{x,p})^2 + \frac{1}{2}(Wk_{y,q})^2. \quad (32)$$

V. SOME AVENUES FOR FUTURE WORK

Since Beltran *et al.* [19, 20] reported signal-to-noise ratio (SNR) boosts of up to 200 in utilising the PM in a tomographic setting, relative to absorption contrast, there has been some interest in the “SNR boosting” properties of the PM [74–77]. Of particular note is the result that the SNR boost has $0.3 \delta/\beta$ as an approximate upper bound under the assumption of Poisson statistics [74, 75], with the SNR boost being even more favourable for very low sample-exposure times [76, 78]. Since dose is proportional to the square of SNR, dose reductions of $300^2 = 90,000$ or more are in principle possible with the PM [76]. This implies that tomographic analyses are possible using much less dose (or, equivalently, much lower acquisition times) than previously required for a single two-dimensional projection. This reduced dose is of importance in the context of medical imaging, while in an industrial-inspection product-quality-control context (or security screening context) it enables significant increases in throughput speed due to the associated increase in source effective-brilliance; cf. e.g. the recent achievement of over 200 x-ray phase-contrast tomograms per second [79], incorporating PM-based data processing. In light of the above comments, it would be interesting to see how the previously published analyses for SNR boost and associated dose reduction are altered by passage from the PM to the GPM. It appears likely that SNR boosts will be reduced somewhat if the GPM is used in place of the PM, in accord with the tradeoff between noise and spatial resolution [80, 81].

Another interesting avenue for future work begins with the previously mentioned observation that, from version 2.1 onwards, the ANKAphase [4] implementation of the PM incorporates a deconvolution mask to boost fine spatial detail in reconstructions. This deconvolution filter $R_{\text{ANKA}}(k_x, k_y)$ takes the Fourier-space form [82]

$$R_{\text{ANKA}}(k_x, k_y) = \frac{1+c}{c + \exp[-\pi\sigma^2(k_x^2 + k_y^2)]}, \quad (33)$$

where c is a dimensionless constant and σ is a characteristic width. In light of the findings of the present paper, it would be interesting to consider replacing the ANKAphase deconvolution filter with

$$\tilde{R}_{\text{ANKA}}(k_x, k_y) = \frac{1+c}{c + \exp[-\sigma^4(k_x^4 + k_y^4)]}, \quad (34)$$

since the fourth-order Taylor expansion of the deconvolution filter would then agree with the fourth-order Taylor

expansion of $R(k_x, k_y)$, provided that

$$\frac{12\sigma^4}{1+c} = W^2\alpha. \quad (35)$$

One more avenue for future research would be to replace Eq. (11), which formed a starting point for the analysis of the present paper, with a more sensitive expression that utilises higher-order discrete approximations to the transverse Laplacian operator. For example, Eq. (25.3.30) of Abramowitz and Stegun [57] makes it clear that, while we have a Taylor-series truncation error on the order of W^2 in the five-point approximation for the Laplacian that is given in Eq. (11), their nine-point approximation in Eq. (25.3.31) [57] gives a better estimate whose truncation error is on the order of W^4 . Use of such higher-order approximations may lead to improved forms of Eq. (17).

We end these indications of possible avenues for future work, by noting that both (i) the two-image TIE-based phase-retrieval method of Paganin and Nugent [83] (see also Sec. 4.5.2 of Paganin [54]), which does not make the assumption of a single-material object, and (ii) the single-image differential-phase-contrast version of the PM [84], which does make such an assumption, would benefit from an analogous treatment of differential operators under the discrete Fourier transform, to that used in the passage from Eqs. (21) to (17). Perhaps the former method (namely that which is based on Ref. [83]) may become of increasing utility in an x-ray imaging setting, given both recent advances in semi-transparent detectors, and the fact that this method does not need the single-material assumption upon which the PM relies.

VI. CONCLUSION

A simple extension was given for the method of Paganin *et al.* [1] (PM), for phase–amplitude reconstruction of single-material samples using a single paraxial x-ray propagation-based phase contrast image obtained under the conditions of small object-to-detector propagation distance. This improves the reconstructed contrast of very fine sample features, using an approximation that is derived from a first-principles perspective. This theoretical investigation was motivated by, and partially explains from a fundamental perspective, the success of several papers incorporating unsharp masking or related techniques to boost fine spatial detail in reconstructions obtained using the PM [4, 10, 43, 47, 50].

ACKNOWLEDGEMENTS

Financial support by the Experiment Division of the ESRF for DMP to visit in 2017 and 2018 is gratefully acknowledged. DMP acknowledges fruitful discussions with Mario Beltran, Carsten Detlefs, Timur Gureyev, Marcus Kitchen, Kieran Larkin, Thomas Leatham, Kaye Morgan, Tim Petersen, James Pollock, Manuel Sánchez del Río and Paul Tafforeau.

[1] D. Paganin, S. C. Mayo, T. E. Gureyev, P. R. Miller, and S. W. Wilkins, Simultaneous phase and amplitude extraction from a single defocused image of a homogeneous object, *J. Microsc.* **206**, 33 (2002).

[2] D. Gabor, A new microscopic principle, *Nature* **161**, 777 (1948).

[3] A. Pogany, D. Gao, and S. W. Wilkins, Contrast and resolution in imaging with a microfocus x-ray source, *Rev. Sci. Instrum.* **68**, 2774 (1997).

[4] T. Weitkamp, D. Haas, D. Wegrzynek, and A. Rack, *ANKAphase*: software for single-distance phase retrieval from inline X-ray phase-contrast radiographs, *J. Synchrotron Radiat.* **18**, 617 (2011).

[5] T. E. Gureyev, Y. Nesterets, D. Ternovski, D. Thompson, S. W. Wilkins, A. W. Stevenson, A. Sakellariou, and J. A. Taylor, Toolbox for advanced x-ray image processing, *Proc. SPIE* **8141**, 81410B (2011).

[6] V. Favre-Nicolin, J. Coraux, M.-I. Richard, and H. Reneyer, Fast computation of scattering maps of nanostructures using graphical processing units, *J. Appl. Cryst.* **44**, 635 (2011).

[7] R.-C. Chen, D. Dreossi, L. Mancini, R. Menk, L. Rigon, T.-Q. Xiao, and R. Longo, *PITRE*: software for phase-sensitive X-ray image processing and tomography reconstruction, *J. Synchrotron Radiat.* **19**, 836 (2012).

[8] M. N. Boone, W. Devulder, M. Dierick, L. Brabant, E. Pauwels, and L. V. Hoorebeke, Comparison of two single-image phase-retrieval algorithms for in-line x-ray phase-contrast imaging, *J. Opt. Soc. Am. A* **29**, 2667 (2012).

[9] M. Dierick, B. Masschaele, and L. Van Hoorebeke, Octopus, a fast and user-friendly tomographic reconstruction package developed in LabView®, *Meas. Sci. Technol.* **15**, 1366 (2004).

[10] A. Mirone, E. Brun, E. Gouillart, P. Tafforeau, and J. Kiesser, The PyHST2 hybrid distributed code for high speed tomographic reconstruction with iterative reconstruction and a priori knowledge capabilities, *Nucl. Instrum. Meth. Phys. Res. B* **324**, 41 (2014).

[11] D. Gürsoy, F. De Carlo, X. Xiao, and C. Jacobsen, TomoPy: a framework for the analysis of synchrotron tomographic data, *J. Synchrotron Radiat.* **21**, 1188 (2014).

[12] D. M. Pelt, D. Gürsoy, W. J. Palenstijn, J. Sijbers, F. De Carlo, and K. J. Batenburg, Integration of TomoPy and the ASTRA toolbox for advanced processing and reconstruction of tomographic synchrotron data, *J. Synchrotron Radiat.* **23**, 842 (2016).

[13] F. Brun, L. Massimi, M. Fratini, D. Dreossi, F. Billé, A. Accardo, R. Pugliese, and A. Cedola, SYRMEP Tomo Project: a graphical user interface for customizing CT reconstruction workflows, *Adv. Struct. Chem. Imaging* **3**, 4 (2017).

[14] L. M. Lohse, A.-L. Robisch, M. Töpperwien, S. Maretzke, M. Krenkel, J. Hagemann, and T. Salditt, A phase-retrieval toolbox for X-ray holography and tomography, *J. Synchrotron Radiat.* **27**, pagination forthcoming (2020).

[15] A. C. Y. Liu, D. M. Paganin, L. Bourgeois, and P. N. H. Nakashima, Projected thickness reconstruction from a single defocused transmission electron microscope image of an amorphous object, *Ultramicroscopy* **111**, 959 (2011).

[16] P. K. Poola and R. John, Label-free nanoscale characterization of red blood cell structure and dynamics using single-shot transport of intensity equation, *J. Biomed. Opt.* **22**, 1 (2017).

[17] D. M. Paganin, M. Sales, P. M. Kadletz, W. Kockelmann, M. A. Beltran, H. F. Poulsen, and S. Schmidt, Effective brilliance amplification in neutron propagation-based phase contrast imaging (2019), arXiv:1909.11186.

[18] S. C. Mayo, T. J. Davis, T. E. Gureyev, P. R. Miller, D. Paganin, A. Pogany, A. W. Stevenson, and S. W. Wilkins, X-ray phase-contrast microscopy and microtomography, *Opt. Express* **11**, 2289 (2003).

[19] M. A. Beltran, D. M. Paganin, K. Uesugi, and M. J. Kitchen, 2D and 3D X-ray phase retrieval of multi-material objects using a single defocus distance, *Opt. Express* **18**, 6423 (2010).

[20] M. A. Beltran, D. M. Paganin, K. K. W. Siu, A. Fouras, S. B. Hooper, D. H. Reser, and M. J. Kitchen, Interface-specific x-ray phase retrieval tomography of complex biological organs, *Phys. Med. Biol.* **56**, 7353 (2011).

[21] S. Mayo, P. Miller, S. W. Wilkins, D. Gao, and T. Gureyev, Laboratory-based x-ray micro-tomography with submicron resolution, in *Developments in X-Ray Tomography V*, Vol. 6318, edited by U. Bonse, International Society for Optics and Photonics (SPIE, 2006) pp. 439–446.

[22] Y. J. Wang, K.-S. Im, K. Fezzaa, W. K. Lee, J. Wang, P. Micheli, and C. Laub, Quantitative x-ray phase-contrast imaging of air-assisted water sprays with high Weber numbers, *Appl. Phys. Lett.* **89**, 151913 (2006).

[23] S. D. Mookhoek, S. C. Mayo, A. E. Hughes, S. A. Furman, H. R. Fischer, and S. van der Zwaag, Applying SEM-based x-ray microtomography to observe self-healing in solvent encapsulated thermoplastic materials, *Adv. Eng. Mater.* **12**, 228 (2010).

[24] S. Yang, D. C. Gao, T. Muster, A. Tulloh, S. Furman, S. Mayo, and A. Trinch, Microstructure of a paint primer - a data-constrained modeling analysis, in *PRICM7*, Materials Science Forum, Vol. 654 (Trans Tech Publications Ltd, 2010) pp. 1686–1689.

[25] C. Blankenburg, A. Rack, C. Daul, and J. Ohser, Torsion estimation of particle paths through porous media observed by in-situ time-resolved microtomography, *J. Microsc.* **266**, 141 (2017).

[26] Y. S. Yang, K. Y. Liu, S. Mayo, A. Tulloh, M. B. Clennell, and T. Q. Xiao, A data-constrained modelling approach to sandstone microstructure characterisation, *J. Petrol. Sci. Eng.* **105**, 76 (2013).

[27] M. A. Denecke, W. de Nolf, A. Rack, R. Tucoulou, T. Vitova, G. Falkenberg, S. Abolhassani, P. Cloetens, and B. Kienzler, Speciation of actinides in granite subjected to tracer studies, in *Actinide Nanoparticle Research*, edited by S. N. Kalmykov and M. A. Denecke (Springer-Verlag, Berlin and Heidelberg, 2011) Chap. 16, pp. 413–435.

[28] K. Uesugi, M. Hoshino, A. Takeuchi, Y. Suzuki, and N. Yagi, Development of fast and high throughput tomography using CMOS image detector at SPring-8, in *Developments in X-Ray Tomography VIII*, Vol. 8506, edited by S. R. Stock, International Society for Optics and Photon-

ics (SPIE, 2012) pp. 90–98.

[29] H. P. Wang, Y. S. Yang, Y. D. Wang, J. L. Yang, J. Jia, and Y. H. Nie, Data-constrained modelling of an anthracite coal physical structure with multi-spectrum synchrotron X-ray CT, *Fuel* **106**, 219 (2013).

[30] R. Mokso, F. Marone, S. Irvine, M. Nyvlt, D. Schwyn, K. Mader, G. K. Taylor, H. G. Krapp, M. Skeren, and M. Stampanoni, Advantages of phase retrieval for fast x-ray tomographic microscopy, *J. Phys. D: Appl. Phys.* **46**, 494004 (2013).

[31] M. Marinescu, M. Langer, A. Durand, C. Olivier, A. Chabrol, H. Rositi, F. Chauveau, T. H. Cho, N. Nighoghossian, Y. Berthezène, F. Peyrin, and M. Wiart, Synchrotron radiation X-ray phase micro-computed tomography as a new method to detect iron oxide nanoparticles in the brain, *Mol. Imaging Biol.* **15**, 552 (2013).

[32] H. Rositi, C. Frindel, M. Langer, M. Wiart, C. Olivier, F. Peyrin, and D. Rousseau, Information-based analysis of X-ray in-line phase tomography with application to the detection of iron oxide nanoparticles in the brain, *Opt. Express* **21**, 27185 (2013).

[33] G. Lovric, S. F. Barré, J. C. Schittny, M. Roth-Kleiner, M. Stampanoni, and R. Mokso, Dose optimization approach to fast X-ray microtomography of the lung alveoli, *J. Appl. Cryst.* **46**, 856 (2013).

[34] A. W. Stevenson, S. C. Mayo, D. Häusermann, A. Maksimenko, R. F. Garrett, C. J. Hall, S. W. Wilkins, R. A. Lewis, and D. E. Myers, First experiments on the Australian Synchrotron Imaging and Medical beamline, including investigations of the effective source size in respect of X-ray imaging, *J. Synchrotron Radiat.* **17**, 75 (2010).

[35] J. Enax, H.-O. Fabritius, A. Rack, O. Prymak, D. Raabe, and M. Epple, Characterization of crocodile teeth: Correlation of composition, microstructure, and hardness, *J. Struct. Biol.* **184**, 155 (2013).

[36] D. A. Schwyn, R. Mokso, S. M. Walker, M. Doube, M. Wicklein, G. K. Taylor, M. Stampanoni, and H. G. Krapp, High-speed x-ray imaging on the fly, *Synchrotron Radiat. News* **26**, 4 (2013).

[37] M. S. Gilani, J. L. Fife, M. N. Boone, and K. G. Wakili, Dynamics of microcrack propagation in hardwood during heat treatment investigated by synchrotron-based X-ray tomographic microscopy, *Wood Sci. Technol.* **47**, 889 (2013).

[38] U. Matsushima, A. Hilger, W. Graf, S. Zabler, I. Manke, M. Dawson, G. Choinka, and W. B. Herppich, Calcium oxalate crystal distribution in rose peduncles: Non-invasive analysis by synchrotron X-ray microtomography, *Postharvest Biol. Technol.* **72**, 27 (2012).

[39] A. McNeil, R. S. Bradley, P. J. Withers, and D. Penney, Imaging fossilised spiders in amber using lab-based phase contrast x-ray tomography, in *Developments in X-Ray Tomography VII*, Vol. 7804, edited by S. R. Stock, International Society for Optics and Photonics (SPIE, 2010) pp. 440–446.

[40] D. Penney, D. I. Green, A. McNeil, R. S. Bradley, Y. M. Marusik, P. J. Withers, and R. F. Preziosi, A new species of *Craspedisus* (Araneae: Theridiidae) in Miocene Dominican amber, imaged using X-ray computed tomography, *Paleontol. J.* **46**, 583 (2012).

[41] G. D. Edgecombe, V. Vahtera, S. R. Stock, A. Kallonen, X. Xiao, A. Rack, and G. Giribet, A scolopocryptopid centipede (Chilopoda: Scolopendromorpha) from Mexican amber: synchrotron microtomography and phylogenetic placement using a combined morphological and molecular data set, *J. Linn. Soc. London, Zool.* **166**, 768 (2012).

[42] H. G. Rodrigues, F. Solé, C. Charles, P. Tafforeau, M. Vianey-Liaud, and L. Viriot, Evolutionary and biological implications of dental mesial drift in rodents: The case of the Ctenodactylidae (Rodentia, Mammalia), *PLoS One* **7**, e50197 (2012).

[43] S. Sanchez, P. E. Ahlberg, K. M. Trinajstic, A. Mirone, and P. Tafforeau, Three-dimensional synchrotron virtual paleohistology: A new insight into the world of fossil bone microstructures, *Microsc. Microanal.* **18**, 1095 (2012).

[44] P. Vršanský, T. van de Kamp, D. Azar, A. Prokin, L. Vidlička, and P. Vagočić, Cockroaches probably cleaned up after dinosaurs, *PLoS One* **8**, e80560 (2013).

[45] Z. Yin, M. Zhu, P. Tafforeau, J. Chen, P. Liu, and G. Li, Early embryogenesis of potential bilaterian animals with polar lobe formation from the Ediacaran Wangan Biota, South China, *Precambrian Res.* **225**, 44 (2013).

[46] K. Trinajstic, S. Sanchez, V. Dupret, P. Tafforeau, J. Long, G. Young, T. Senden, C. Boisvert, N. Power, and P. E. Ahlberg, Fossil musculature of the most primitive jawed vertebrates, *Science* **341**, 160 (2013).

[47] S. Sanchez, V. Dupret, P. Tafforeau, K. M. Trinajstic, B. Ryll, P.-J. Gouttenoire, L. Wretman, L. Zylberberg, F. Peyrin, and P. E. Ahlberg, 3D microstructural architecture of muscle attachments in extant and fossil vertebrates revealed by synchrotron microtomography, *PLoS One* **8**, e56992 (2013).

[48] S. E. Pierce, P. E. Ahlberg, J. R. Hutchinson, J. L. Molnar, S. Sanchez, P. Tafforeau, and J. A. Clack, Vertebral architecture in the earliest stem tetrapods, *Nature* **494**, 226 (2013).

[49] For a partial list of additional references that use the ANKAPhase implementation [4] of the phase-retrieval algorithm of Paganin *et al.* [1], see e.g. <http://www.alexanderrack.eu/ANKAPhase/ankaphase.users.html>.

[50] S. Irvine, R. Mokso, P. Modregger, Z. Wang, F. Marone, and M. Stampanoni, Simple merging technique for improving resolution in qualitative single image phase contrast tomography, *Opt. Express* **22**, 27257 (2014).

[51] We use the term “Lorentzian” to refer to functions of the form $f(x, a) = 1/(a^2 + x^2)$, where a is a real non-zero constant and x is real variable. Note, however, that such functions are also often referred to as Breit–Wigner distributions or Cauchy distributions.

[52] B. Yu, L. Weber, A. Pacureanu, M. Langer, C. Olivier, P. Cloetens, and F. Peyrin, Phase retrieval in 3D X-ray magnified phase nano CT: Imaging bone tissue at the nanoscale, in *2017 IEEE 14th International Symposium on Biomedical Imaging (ISBI 2017)* (2017) pp. 56–59.

[53] M. R. Teague, Deterministic phase retrieval: a Green’s function solution, *J. Opt. Soc. Am.* **73**, 1434 (1983).

[54] D. M. Paganin, *Coherent X-Ray Optics* (Oxford University Press, Oxford, 2006).

[55] D. Paganin, T. E. Gureyev, S. C. Mayo, A. W. Stevenson, Y. I. Nesterets, and S. W. Wilkins, X-ray omni microscopy, *J. Microsc.* **214**, 315 (2004).

[56] W. H. Press, S. A. Teukolsky, W. T. Vetterling, and B. P. Flannery, *Numerical Recipes in FORTRAN: The Art of Scientific Computing*, 2nd ed. (Cambridge Uni-

versity Press, 1996).

[57] M. Abramowitz and I. A. Stegun, *Handbook of Mathematical Functions with Formulas, Graphs, and Mathematical Tables* (National Bureau of Standards Applied Mathematics Series, Washington DC, 1964).

[58] K. R. Freischlad and C. L. Koliopoulos, Modal estimation of a wave front from difference measurements using the discrete Fourier transform, *J. Opt. Soc. Am. A* **3**, 1852 (1986).

[59] D. C. Ghiglia and L. A. Romero, Robust two-dimensional weighted and unweighted phase unwrapping that uses fast transforms and iterative methods, *J. Opt. Soc. Am. A* **11**, 107 (1994).

[60] M. R. Arnison, K. G. Larkin, C. J. R. Sheppard, N. I. Smith, and C. J. Cogswell, Linear phase imaging using differential interference contrast microscopy, *J. Microsc.* **214**, 7 (2004).

[61] W. H. Richardson, Bayesian-based iterative method of image restoration, *J. Opt. Soc. Am.* **62**, 55 (1972).

[62] L. B. Lucy, An iterative technique for the rectification of observed distributions, *Astron. J.* **79**, 745 (1974).

[63] P. Cloetens, W. Ludwig, J. Baruchel, D. Van Dyck, J. Van Landuyt, J. P. Guigay, and M. Schlenker, Holotomography: Quantitative phase tomography with micrometer resolution using hard synchrotron radiation x rays, *Appl. Phys. Lett.* **75**, 2912 (1999).

[64] T. E. Gureyev, T. J. Davis, A. Pogany, S. C. Mayo, and S. W. Wilkins, Optical phase retrieval by use of first Born- and Rytov-type approximations, *Appl. Opt.* **43**, 2418 (2004).

[65] T. E. Gureyev, A. Pogany, D. M. Paganin, and S. W. Wilkins, Linear algorithms for phase retrieval in the Fresnel region, *Opt. Commun.* **231**, 53 (2004).

[66] L. D. Turner, B. B. Dhal, J. P. Hayes, A. P. Mancuso, K. A. Nugent, D. Paterson, R. E. Scholten, C. Q. Tran, and A. G. Peele, X-ray phase imaging: Demonstration of extended conditions with homogeneous objects, *Opt. Express* **12**, 2960 (2004).

[67] B. Yu, L. Weber, A. Pacureanu, M. Langer, C. Olivier, P. Cloetens, and F. Peyrin, Evaluation of phase retrieval approaches in magnified X-ray phase nano computerized tomography applied to bone tissue, *Opt. Express* **26**, 11110 (2018).

[68] M. A. Beltran, D. M. Paganin, and D. Pelliccia, Phase- and-amplitude recovery from a single phase-contrast image using partially spatially coherent x-ray radiation, *J. Opt.* **20**, 055605 (2018).

[69] T. E. Gureyev, A. W. Stevenson, Ya. I. Nesterets, and S. W. Wilkins, Image deblurring by means of defocus, *Opt. Commun.* **240**, 81 (2004).

[70] H. Risken, *The Fokker-Planck Equation: Methods of Solution and Applications*, 2nd ed. (Springer Verlag, Berlin, 1989).

[71] K. S. Morgan and D. M. Paganin, Applying the Fokker-Planck equation to x-ray grating-based phase and dark-field imaging, *Sci. Rep.* **9**, 17465 (2019).

[72] D. M. Paganin and K. S. Morgan, X-ray Fokker-Planck equation for paraxial imaging, *Sci. Rep.* **9**, 17537 (2019).

[73] See, in particular, the special case of Eq. (59) in the paper by Paganin and Morgan [72], in which their “effective diffusion coefficient” $D_{\text{eff}}(x, y)$ is considered to be independent of transverse coordinates (x, y) . The resulting Fokker-Planck equation is mathematically identical in form to the screened Poisson equation given when Eq. (9) of the main text is modified by the replacement that is indicated in Eq. (30).

[74] Y. I. Nesterets and T. E. Gureyev, Noise propagation in x-ray phase-contrast imaging and computed tomography, *J. Phys. D: Appl. Phys.* **47**, 105402 (2014).

[75] T. E. Gureyev, S. C. Mayo, Y. I. Nesterets, S. Mohammadi, D. Lockie, R. H. Menk, F. Arfelli, K. M. Pavlov, M. J. Kitchen, F. Zanconati, C. Dullin, and G. Tromba, Investigation of the imaging quality of synchrotron-based phase-contrast mammographic tomography, *J. Phys. D: Appl. Phys.* **47**, 365401 (2014).

[76] M. J. Kitchen, G. A. Buckley, T. E. Gureyev, M. J. Wallace, N. Andres-Thio, K. Uesugi, N. Yagi, and S. B. Hooper, CT dose reduction factors in the thousands using x-ray phase contrast, *Sci. Rep.* **7**, 15953 (2017).

[77] T. E. Gureyev, Y. I. Nesterets, A. Kozlov, D. M. Paganin, and H. M. Quiney, On the “unreasonable” effectiveness of Transport of Intensity imaging and optical deconvolution, *J. Opt. Soc. Am. A* **34**, 2251 (2017).

[78] L. Clark, T. C. Petersen, T. Williams, M. J. Morgan, D. M. Paganin, and S. D. Findlay, High contrast at low dose using a single, defocussed transmission electron micrograph, *Micron* **124**, 102701 (2019).

[79] F. García-Moreno, P. H. Kamm, T. R. Neu, F. Bülk, R. Mokso, C. M. Schlepütz, M. Stampanoni, and J. Banhart, Using X-ray tomoscopy to explore the dynamics of foaming metal, *Nat. Commun.* **10**, 3762 (2019).

[80] T. E. Gureyev, Ya. I. Nesterets, F. de Hoog, G. Schmalz, S. C. Mayo, S. Mohammadi, and G. Tromba, Duality between noise and spatial resolution in linear systems, *Opt. Express* **22**, 9087 (2014).

[81] T. E. Gureyev, A. Kozlov, D. M. Paganin, Ya. I. Nesterets, and H. M. Quiney, Noise-resolution uncertainty principle in classical and quantum systems, *Sci. Rep.* (2020), accepted paper in press.

[82] See <https://imagej.nih.gov/ij/plugins/ankaphase/ankaphase-userguide.html> for an updated form of the ANKAphase software, which extends the form reported in Weitkamp *et al.* [4], to incorporate the optional image-restoration deconvolution filter that is reproduced in Eq. (33) of the main text.

[83] D. Paganin and K. A. Nugent, Noninterferometric phase imaging with partially coherent light, *Phys. Rev. Lett.* **80**, 2586 (1998).

[84] D. Paganin, T. E. Gureyev, K. M. Pavlov, R. A. Lewis, and M. Kitchen, Phase retrieval using coherent imaging systems with linear transfer functions, *Opt. Commun.* **234**, 87 (2004).